DOI:10.1190/INT-2021-0195.1

A new approach to processing and imaging multibeam water column echosounder data: Application to a complex methane seep on the southern Cascadia margin

Anne M. Tréhu[1], Jeffrey W. Beeson[2], and Susan G. Merle[2]

Abstract

Acoustic echosounding systems are increasingly used to image water-column backscatter in addition to mapping the seafloor. We have imaged an acoustic flare generated by methane bubbles emanating from a vent sourced at 1840 m water depth offshore northern California using a shipboard Kongsberg EM122. Data include five transits over the flare and approximately 11 h of continuous observation when the ship held station. Shipboard observations showed a strong flare splitting into multiple smaller, intermittent flares at a water depth of 800–1200 m and pronounced temporal variability. We introduce a new approach to processing the data in which we correct the backscatter data for ship motion and bin the data into voxels with dimensions of 20 m in X and Y and 40 m in Z for a transit over the flare and into vertical slices with dimensions of 15 m in X and Z and 4 min in time when the ship was stationary. The processed data indicate that the signal is dominated by bubbles emanating from a source region with a diameter of approximately 40 m located on the southern edge of what is likely a ring of sources with a diameter of approximately 600 m. When the ship was stationary, we were able to track an individual pulse rising at a rate of 8–10 m/min. Our results illustrate the limitations of monitoring temporal variation in gas flux using multibeam echosounders because of the trade-off between imaging the entire flare by averaging over tens of minutes to hours and observing a slice through the flare to capture short-lived pulses of gas expulsion. Nevertheless, because echosounders are widely available, they can continue to provide valuable data on the spatial and temporal distribution of gas emissions on continental margins that can be used to frame hypotheses and plan more comprehensive follow-up experiments.

Introduction

Many observations of seafloor vent systems indicate that gas bubbles are released from the seafloor into the ocean. Determining whether these bubbles are dissolved in the ocean or whether they can traverse the ocean to enter the atmosphere is important for evaluating the impact of this gas source on climate (e.g., Dickens, 2011; Ruppel and Kessler, 2017). Acoustic backscatter from within the ocean measured with single or multibeam echosounding (MBES) systems is widely used for mapping and imaging streams of bubbles rising from the seafloor on continental margins and from submarine volcanoes worldwide (e.g., Merewether et al., 1985; Hornafius et al., 1999; Leifer and Patro, 2002; Heeschen et al., 2003; Westbrook et al., 2009; Kannberg et al., 2013; Berndt et al., 2014; Chadwick et al., 2014; Veloso et al., 2015; Philip et al., 2016; Römer et al., 2016; Biggs et al., 2019; Razaz et al., 2020; Merle et al., 2021). The acoustic backscatter images are generally referred to as "flares" in recognition of their flame-like appearance. Because these tools are widely available on research vessels, much of the acoustic backscatter data to image flares has been obtained as a "bonus" during cruises designed primarily to address other objectives. Where the gas composition has been verified through analysis of samples, the primary gas on continental margin vents has been methane (e.g., Hovland et al., 1995; Heeschen et al., 2005; Baumberger et al., 2018), whereas it is dominantly carbon dioxide in volcanic environments (Chadwick et al., 2014).

In most studies, flares have been observed as a ship passes over them. Although seafloor observations indi-

[1]Oregon State University, College of Earth, Ocean, and Atmospheric Sciences, Corvallis, Oregon 97331-5503, USA. E-mail: anne.trehu@oregonstate.edu.

[2]Cooperative Institute for Marine Ecosystem and Resources Studies — Oregon State University, and NOAA PMEL Earth Ocean Interactions Program, Newport, Oregon 97365, USA. E-mail: jeff.beeson@noaa.gov (corresponding author); susan.merle@noaa.gov.

Manuscript received by the Editor 2 October 2021; published online 24 February 2022. This paper appears in *Interpretation*, Vol. 10, No. 1 (February 2022); p. SB93–SB106, 10 FIGS.

http://dx.doi.org/10.1190/INT-2021-0195.1.

cate that individual bubbling vents are ephemeral (e.g., Tryon et al., 1999), repeat surveys have suggested that the general locations where flares are observed may remain stable on a decadal time scale (e.g., Kannberg et al., 2013), and geochemical analyses of carbonates associated with methane vents suggest stability on a millennial time scale (e.g., Teichert et al., 2003; Berndt et al., 2014; Gwiazda et al., 2016; Prouty et al., 2016). A few acoustic studies have used shipboard echosounders to image temporal variation in methane flux on times scales of minutes to months and show considerable temporal variation in acoustic flare intensity (e.g., Salmi et al., 2011; Kannberg et al., 2013; Philip et al., 2016).

To obtain quantitative estimates of variations in methane flux and the factors that drive the variation requires long observation time (months to years) and rapid sampling rates using a variety of optical and multifrequency acoustic sensors. For example, Römer et al. (2016) report results from a year of acoustic backscatter observations at 250 kHz of an active bubbling vent at hourly intervals on the Cascadia margin at 1250 m depth offshore Vancouver Island and correlate those observations with observations of seafloor pressure, temperature, and other parameters. They observe strong temporal variability in gas emission rate, with periods of nearly continuous activity and periods of relative quiet punctuated by occasional bursts of activity. They also note a strong correlation with tides, with the onset of gas emission generally occurring with a falling tide and longer period variability corresponding to changes in oceanographic conditions. They do not see any correlation with bottom pressure signals indicative of regional and teleseismic earthquakes. When they transit over the site with a split beam echosounder with five frequencies ranging from 18 to 200 kHz, they note that the flares are brightest at 18 kHz, reflecting the dominant size of bubbles. Razaz et al. (2020) report on seafloor optical observations made at 6 h intervals for 153 days at a vent at 1080 m depth in the Gulf of Mexico and integrated with various acoustic and satellite observations and models to quantify the relationship between bubble extrusion at the seafloor and satellite observations of oil slicks on the sea surface.

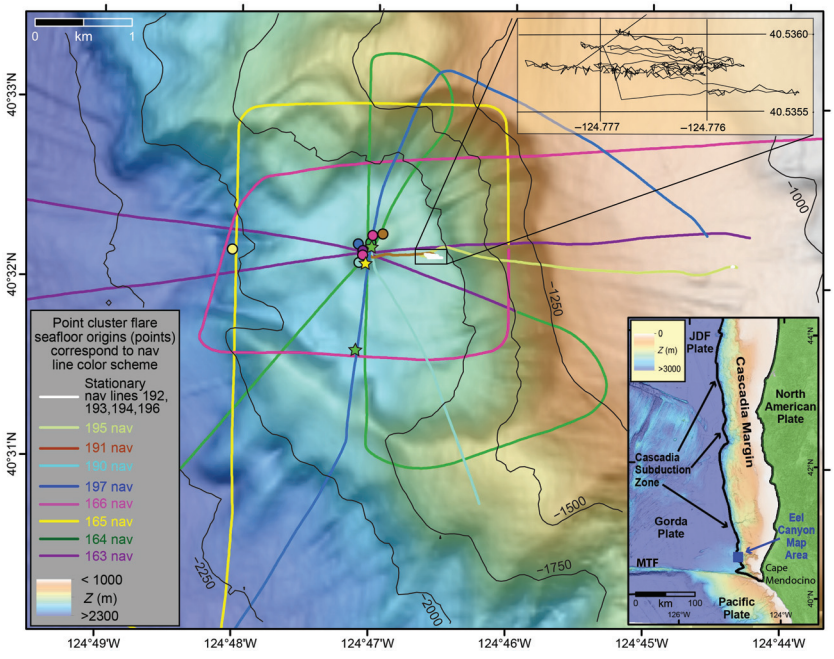

Figure 1. Bathymetric map of the continental margin in the vicinity of the Eel Canyon flare. Track lines from cruise AT26-02 that were used for this study are shown. Lower right inset shows the tectonic setting (MTF, Mendocino transform fault; JDF, Juan de Fuca). Circles show emergence points of flares projected to the seafloor and color coded to correspond to the lines on which they were observed. All but one of the flares observed originated on a mound in the middle of a heart-shaped slide scar at a depth of approximately 1840 m. Line labeling corresponds to file numbers. Lines 163–166 were acquired on 2 July 2013, when we surveyed the site to determine whether the flare reported by Gardner et al. (2009) was still active. Lines 190–196 were acquired on 3 July 2013, when we returned to the site to observe it from a stationary and offset position, as discussed in the text. Line 197 was acquired as we transited over the site. The yellow star shows where bubbles, abundant vent-related fauna, and massive hydrate were observed during dive H1668 (NA095 cruise report, 2018). Green stars show locations of XBT casts during transit 197 shown in Figure 10b. The track line for the period of time when the ship was approximately stationary is in white and is shown in detail in the upper right inset. Bathymetric contours are at 250 m intervals.

In this paper, we discuss data from a cruise during which the shipboard Kongsberg EM122 12 kHz MBES system was used as a tool of opportunity to acquire time-series observations of water column backscatter over a previously identified flare (Gardner et al., 2009) located in the accretionary complex of the Cascadia subduction zone in 1840 m water depth near the base of the slope at the southern end of the Cascadia subduction zone (Figure 1 inset). The opportunity arose when weather conditions during cruise AT26-02 (AT26-02 Science Party, 2013) were too rough for the primary cruise objective of recovering ocean-bottom seismometers (OBSs) that had been deployed nearby. Once the presence of an acoustic flare at the previously reported site was confirmed, we imaged changes in its character and intensity for several hours by holding a station near its source. This provided snapshots of approximately the same slab through the flare at 12 s intervals.

Figure 2a shows an example of the flare discussed in this paper as seen in the real-time shipboard display, and Figure 2b and 2c schematically shows some of the factors that must be considered when interpreting such images of acoustic backscatter. These include the limited volume illuminated by the acoustic beams, which can lead to truncation of the image from above or below as the flare is deflected by ocean currents and internal waves and bubbles move in and out of the imaged slice. To prevent

DOI:10.1190/INT-2021-0195.1

DOI:10.1190/INT-2021-0195.1

bubbles from dissolving rapidly as they enter the ocean, which is undersaturated in methane, they must be armored to isolate the gas from the ocean, either by a gas hydrate shell that forms on contact with the ocean or by a coating of the bubbles by liquid hydrocarbons or a biofilm. It is also important to consider that a narrow-band acoustic source will be sensitive to a narrow range of bubble sizes (e.g., Clay and Medwin, 1977; Leifer and Patro, 2002; Rehder et al., 2009; Veloso et al., 2015; Biggs et al., 2019), that bubble size will increase as the bubbles rise and pressure decreases (thus affecting the backscatter intensity), and that gas exsolution in response to depressurization can form bubbles as aqueous vent fluids rise through the ocean. Other scattering sources, such as plankton and schools of fish, must also be distinguished from acoustic flares resulting from bubbles emanating from the seafloor. Here, we focus on the challenge of separating rapid (minutes to hours) temporal changes in bubble flux from changes due to motion of the ship or ocean currents to obtain insights into the temporal and spatial characteristics of a particularly bright flare. We do not attempt to quantify absolute fluxes because of the many confounding factors mentioned previously.

Background

The thickly sedimented Juan de Fuca (JDF) plate is subducted beneath North America at the Cascadia subduction zone. These sediments, which are primarily of terrestrial origin, contain a relatively high concentration of organic matter, which decomposes to form methane. In response to subduction, some of the sediment is accreted to the North American plate at the deformation front, forming an accretionary wedge along the edge of the plate; some is subducted several kilometers beneath this wedge before being underplated to the base of the wedge; and some is subducted to greater depth (e.g., Hyndman et al., 1993; Tréhu et al., 1995, 1999; Gulick et al., 1998; Adam et al., 2004; Fisher et al., 2005). The complex fluid flow pathways for methane-rich pore fluids created by these processes result in focusing of fluids, exsolution of methane in response to decreasing pressure, widespread presence of gas hydrate in the subsurface, and generation of localized vents in which free gas is expelled from the seafloor into the ocean (e.g., Suess et al., 2001; Torres et al., 2002, 2004, 2009; Heeschen et al., 2003, 2005; Tréhu et al., 2004, 2006; Phrampus et al., 2017). Such vents are widespread along Cascadia (Riedel et al., 2018); most originate in water depth shallower than 1000 m, although they have been observed to originate as deep as 2043 m below the sea surface (Merle et al., 2021).

For water depths greater than approximately 500 m in Cascadia, pressure and temperature conditions are within the stability field for methane hydrate formation within the shallow sediments and near-bottom ocean waters. Gas hydrate formation in the subsurface is a mechanism for trapping and storing methane in the sediments, which will be released if temperature or pressure conditions move outside the range necessary for hydrate stability. The presence of methane bubbles emanating from the seafloor within the methane hydrate stability field (MHSF) indicates that methane is present in the pore waters in a concentration that exceeds the solubility of methane at ambient temperature and pressure and either that the free gas thus released is mechanically isolated from water or that the stability field has been perturbed by changes in pore-water chemistry (e.g., Leifer and Patro, 2002; Tréhu et al., 2004; Rehder et al., 2009).

The number of flares observed on the Cascadia margin decreases rapidly as water depth increases (Riedel et al., 2018; Merle et al., 2021). This is likely due to the pressure dependence of the solubility of methane in water. The abundance of methane at this site is likely due to the extremely high sedimentation rate on the

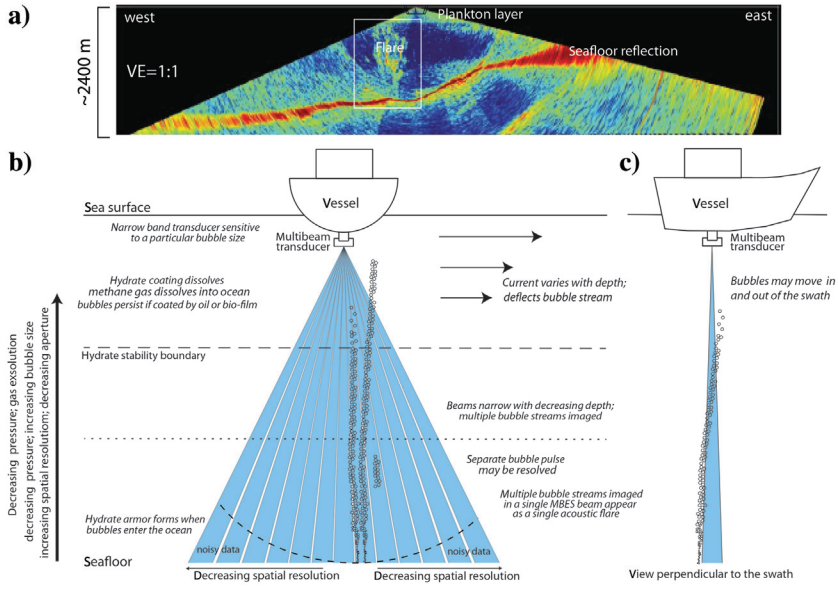

Figure 2. (a) Example of the Eel Canyon flare as observed on the shipboard display. The signal from a single ping recorded on 288 beams is shown. Reflections are recorded from a swath of seafloor perpendicular to the ship track with a maximum aperture of approximately 8 km. Water depth increases from east to west with a depth of 1840 m beneath the ship in this image. Backscatter from within the water column within a radius that is approximately equal to the water depth beneath the ship is also recorded with a good S/N. The white box outlines the part of the backscatter signal that is processed to generate the images discussed here. (b) Schematic illustration of some of the factors that affect the appearance of a flare or flare cluster in a swath view. Aperture increases, but resolution decreases with increasing water depth and distance from the center beam. This changing geometry must be considered when interpreting the data. The narrow frequency band of the transmitted MBES energy also affects the appearance of the flare. (c) Schematic illustration of a side view of a swath showing how a flare may enter and exit from the ensonified volume.

abyssal plain seaward of the deformation front as evidenced by seismic reflection and refraction data, which indicate that the 7-million-year-old lithosphere of the southeast corner of the JDF plate adjacent to the Mendocino transform fault (MTF) is flexed down under the load of approximately 8 km of terrigenous sediment (Godfrey et al., 1998; Henstock and Levander, 2003). This is several times thicker than the sediment approaching the deformation front elsewhere in Cascadia, which ranges from approximately 1.2 to 4 km (Wang and Tréhu, 2016). The very high sedimentation rate offshore Cape Mendocino results in transport of a considerable amount of organic material to the lower slope and abyssal plain, providing abundant source material for gas generation.

Methane is a powerful greenhouse gas, and whether the methane expelled from the seafloor reaches the sea surface and enters the atmosphere is important for evaluating the impact of this methane source on climate change. In the Gulf of Mexico, oil slicks observed on the sea surface where acoustic flares rise from the seafloor to the sea surface indicate that a film of oil armors the bubbles (MacDonald et al., 2002, 2015). In Cascadia, nearly all flares reported to date that originate where the seafloor is deeper than approximately 600 m fade rapidly greater than 500 m water depth (Heeschen et al., 2003; Kannberg et al., 2013; Philip et al., 2016; Riedel et al., 2018; Merle et al., 2021), although some vigorous flares remain detectable above the background noise for several hundred meters above the MHSF. This has been interpreted to indicate that bubbles are armored by hydrate as they emerge from the seafloor and dissolve as this armor dissociates when the bubble rises above the MHSF. Given the depth at which the Eel River Basin flare discussed in this paper originates, it is likely that very little, if any, of the methane released here reaches the atmosphere (Ruppel and Kessler, 2017).

An energetic and complex acoustic flare caused by methane emissions emanating from the seafloor at a depth of 1840 m on the southern Cascadia margin was discovered in 2009 (Gardner et al., 2009). It was vigorous when we returned to the site in 2013 to image it acoustically and when it was visited in 2011 and 2018 with an autonomous underwater vehicle or remotely operated vehicle (ROV), seafloor cameras, and seafloor sediment and fluid samplers (Gwiazda et al., 2016; NA095 cruise report, 2018), suggesting that these systems remain active over time periods of years. Gwiazda et al. (2016) find up to 50 m of sediment drape covering much of the floor of the slump scar and do not find any fresh outcrops along its headwall, leading them to conclude that the slide was old and currently inactive. However, no subsurface reflections were observed in Chirp profiles beneath an approximately 60 m high, 350 m wide, and 650 m long mound on the floor of the slump, which has the rough topography characteristic of other methane seeps in which methane-derived authigenic carbonates and massive gas hydrate deposits have been found (e.g., Suess et al., 2001; Kannberg et al., 2013; Paull et al., 2015). Thermogenic gas containing methane and up to 5% higher order hydrocarbons with no recent biogenic contribution was sampled from the mound (Gwiazda et al., 2016). Liquid hydrocarbon droplets were also observed. The site was revisited in 2018 by ROV dive H1668 during cruise NA095-002 (NA095 cruise report, 2018). Bubbles, abundant vent-related fauna, and massive hydrate were observed at the seafloor at the location shown by a yellow star in Figure 1, which corresponds closely to the flare origins discussed in this paper when projected onto the seafloor. Unfortunately, no deep penetration seismic reflection data cross the Eel Canyon slump; consequently details of the plumbing system that transports methane-rich pore fluids to the seafloor at this location cannot be reconstructed. This segment of the Cascadia deformation front is characterized by a large number of slope failure scars (Hill et al., 2020), perhaps because of frequent strong shaking due to its proximity to the very active transform segment of the Mendocino fracture zone as well as to the Cascadia subduction zone (Figure 1).

Data acquisition

During cruise AT26-02, time-series observations were acquired over several flares on the Cascadia margin (Figure 1). Although the primary objective of the cruise was to recover OBSs deployed for the Cascadia Initiative (Toomey et al., 2014), we recorded approximately 20 h (0500–1100 on 2 July and 0200–1600 on 3 July 2013) of acoustic backscatter data over a flare originating at 1840 m below the sea surface on the southern Cascadia margin. Both windows of data acquisition occurred while waiting for sea state conditions to improve enough to allow us to continue OBS recoveries (AT26-02 Science Party, 2013). Data were recorded using a hull-mounted Kongsberg EM122 swath multibeam echosounder with 288 beams. Ping interval was approximately 10 s, and useful swath width (Figure 2a) was approximately twice the water depth. Acoustic Doppler current profiler (ADCP) data (75 kHz) and expendable bathythermograph (XBT) data were also acquired as part of the standard shipboard measurement suite, providing information on ocean currents, temperature, and sound velocity (AT26-02 Science Party, 2013). Although the MBES data quality undoubtedly was also impacted by the rough seas at this time because of bubbles trapped beneath the hull and pitching and rolling of the ship, signal-to-noise ratio (S/N) was adequate to find and monitor a vigorous flare that had previously been reported by Gardner et al. (2009).

On 2 July, four transects were acquired over the flare at a speed of 4 knots and from different azimuths. On 3 July, the ship was positioned over the flare for approximately 2 h and then moved approximately 800 m east of the flare's origin on the seafloor to provide an oblique viewing angle with a direct "line of sound" to the flare from top to bottom. This experimental geometry provided a continuous, but incomplete, view of the flare because the MBES swath is wide in the plane perpendicular

DOI:10.1190/INT-2021-0195.1

to the ship's axis but narrow parallel to it, providing data for a vertical slice through the flare with potentially high-resolution information on temporal change. The location of the vertical slice through the ocean varied with time as the ship's heading changed, a factor that must be considered when interpreting temporal change in the data. This experimental approach complements the strategy of making multiple transits over the vent field (Kannberg et al., 2013; Chadwick et al., 2014; Philip et al., 2016), which provides backscatter images of flares that are spatially averaged over tens of minutes. It had the benefit of also allowing us to keep headed into the seas, minimizing pitching and rolling of the ship, which improved the comfort of all aboard as well as improved the data quality. As OBS recovery operations were resumed, we acquired a fifth transit over the vent at 4 knots.

Data processing and description

Transects over the flare

MBES data were examined and processed using proprietary quality positioning services (QPS) FMMidwater software. The first stage of processing entails interactive replay of the data and application of different amplitude clipping functions to visualize the large dynamic range present in the backscatter and identify time periods of particular interest. On input into FMMidwater, the data are georeferenced assuming that the speed of sound through the ocean is constant and equal to the speed measured at the ship's transducer; data are not corrected for the ship's pitch and roll. Figure 3 shows how the appearance of the flare changed, as displayed with FMMidwater, during a transit over the flare at a speed of 4 knots along a north–south track (Figure 1, line 197). Seven pings spaced 1 min apart illustrate how the intensity of the flare varied rapidly during the transit. All seven snapshots in Figure 3 are shown with the same backscatter amplitude scale. In addition, the snapshot at 16:20 is also shown with a lower gain to illustrate the effect of changing the clipping parameters and shows variations in amplitude with depth within the flare where the intensity is greatest. The flare was visible above background for approximately 10 min, corresponding to a distance of approximately 1200 m along the ship track. The low-gain image shows the rapid decrease in backscatter amplitude greater than approximately 500 m, consistent with the idea that armoring of bubbles by a gas hydrate shell is an important mechanism that allows bubbles to rise through the water column, from deep vents, and that much of this gas is dissolved before it reaches the atmosphere (Heeschen et al., 2003; Ruppel and Kessler, 2017). Although the flare is hundreds of meters wide in the depth range of approximately 500–1400 m, it can only be tracked to the seafloor for approximately 20 s during transit, which corresponds to approximately 40 m on the seafloor (Figure 3 at 16:21).

A common approach to this type of data is to generate point clusters representing high-backscatter intensity that can be visualized in three dimensions (e.g., Gardner et al., 2009; Veloso et al., 2015; Philip et al., 2016; Razaz et al., 2020). We generated point clusters using FMMidwater by averaging backscatter intensity within user-specified volume elements and applying a threshold intensity to define a point; the resultant display thus depends on subjective threshold parameters. Figure 4 shows a 3D perspective view of the seafloor topography and point clusters representing high-backscatter intensity in the overlying water column generated from five transects acquired at 4 knots with different orientations across the Eel Canyon (Figure 1). The point clusters derived from each transect are represented by different colors. Four of the transects (lines 163–166) were acquired between 0500 and 1100 GMT on 2 June 2013, to determine whether the flare reported by Gardner et al. (2009) was still active. In general, the flare occupies a similar volume of ocean during the four transects acquired on June 2 (lines 163–166). By the time line 190 was acquired, it had shifted slightly to the west, and it continued to shift northwest between lines 190 and 197, which is the time period when the

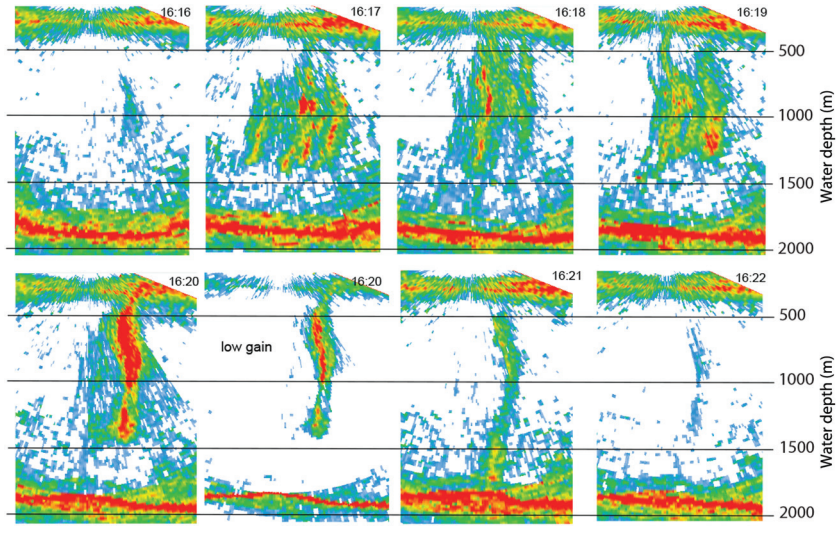

Figure 3. Snapshots of a flare displayed and processed using FMMidwater at 1 min intervals as the ship steamed over the Eel Canyon slump at 4 knots. The numbers in the upper right of each image are the hour and minute on 3 July 2013. All images are shown with approximately the same horizontal and vertical scales and with the same gain with the exception of the image for 1620 labeled "low gain," which is included to illustrate the large dynamic range in backscatter intensity. The red area shows the highest backscatter intensity, with intensity decreasing to yellow, green, and blue. White areas have intensity below the threshold value chosen to highlight the flare. The entire flare was covered in approximately 10 min (approximately 1200 m along track). Although the flare occupies a large volume in the depth range of approximately 600–1400 m, the connection to the seafloor is only very briefly imaged.

DOI:10.1190/INT-2021-0195.1

flare was observed from a stationary viewpoint. Although the backscatter amplitude used to define the point clusters does not show the flares extending to the seafloor, individual columns of relatively high backscatter can be detected by manually scanning through the data in FMMidwater to track seafloor backscatter anomalies to the seafloor, resulting in the apparent bubble emergence sites on the seafloor indicated in Figures 1 and 4. Most of the bubble emergence sites are located near the southwest end of the elongate topographic mound located within the Eel Canyon slump (Figure 1).

The next stage of processing, using QPS Qimera software, entailed integration of the backscatter data with the ship's navigation data, including heading, pitch, and roll as well as geographic position, to place the backscatter results in a 3D geographic reference frame. Ray tracing based on a local sound velocity profile (measured by XBT for this study; AT26-02 Science Party, 2013) was also implemented to improve positioning of the backscattered energy in 3D. All backscatter values from within a specified volume of interest were saved. Georeferenced backscatter intensities were then binned into voxels using Python, and the mean backscatter intensity in each voxel was determined. This process generated an opaque data volume analogous to a 3D seismic tomography model that can be displayed as arbitrarily oriented slices through the data volume. We conducted several tests to determine the voxel dimensions that were best for retaining resolution while improving S/N. Figure 5 shows results for a horizontal slice through the water column with its base at 1200 m for different voxel sizes. Increasing the thickness from 20 to 40 m for voxels that are 20 × 20 m in the horizontal plane fills in many of the holes in the coverage. Increasing the thickness of the slice to 60 m did not visibly improve the coverage or S/N, and increasing the horizontal voxel dimensions to 40 × 40 m resulted in a blurred image. We therefore decided to use a voxel size of 20 × 20 × 40 m for visualizing the backscatter observed during transit line 197.

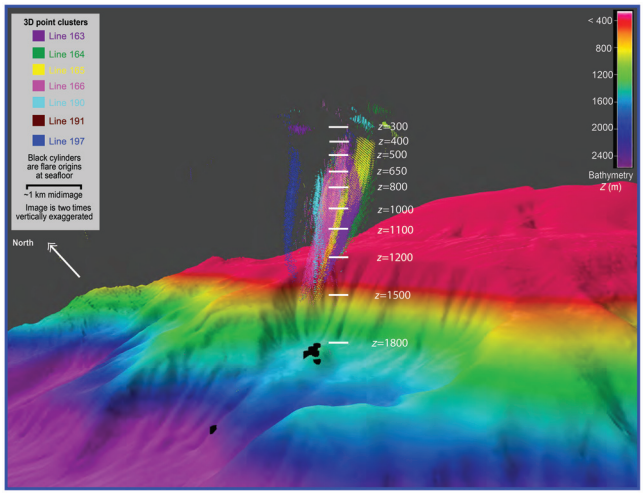

Figure 4. Point clusters from five different crossings of the Eel Canyon slump flare. The ship tracks for each of these crossings are shown in Figure 1. Because only the strongest backscatter is used to define points, this image does not show the flares extending to the seafloor. The flare origins on the seafloor were traced by scanning through the data as discussed in the text and illustrated in Figure 3. Most of the flares can be traced to a distinct mound on the floor of the slump and may include several different vents where bubbles and liquid hydrocarbons have been observed and sampled (Gwiazda et al., 2016; NA9502 cruise report, 2018).

Horizontal slices showing backscatter from the ocean at intervals of 200 m from 1600 to 400 m below the sea surface are shown in Figure 6; the seafloor bathymetry and backscatter intensity are also shown. Supplemental file S1 is an animation that shows the depth-dependent change in backscatter in more detail. At 1600 m, the flare appears to be a column with a diameter of approximately 50 m that overlies the southwestern end of the seafloor mound. In Figure 6, we use this position of the flare at 1600 m as a reference for tracking its position with depth. At a water depth of 1400 m, the diameter of the central core of the flare has grown to approximately 100 m and its center has shifted approximately 50 m to the north. At a water depth of 1200 m, the diameter has further increased, the edges are irregular, and the center has shifted approximately 50 m to the northwest. Between 1200 and 600 m, the flare appears to rise vertically. As noted in Figure 4, the amplitude of the flare decreases rapidly above approximately 500 m, and it is no longer distinct in the slice at 400 m. Northeast of the primary core of the flare, several high-amplitude streaks that trend northwest–southeast and north–south are observed. These streaks are brightest between 1200 and 800 m, but they are also present at 1400 and 600 m in Figure 6 and can be seen emerging from the background noise as deep as 1600 m in the animation. These are likely secondary flares resulting from multiple bubble-emitting vents that were less vigorous than the primary vent during our observation period. Although it is difficult to identify individual flares in Figure 6, a general northwest drift of these secondary flares is apparent in the animation. The seafloor reflectivity derived from the MBES data is not anomalously high beneath the flare, and seafloor bright spots are observed elsewhere on the floor of the canyon, suggesting that the locus of venting moves over long time periods.

Continuous monitoring while holding station

The character of the flare changed dramatically during the time period when the ship held station, as shown in snapshots from single pings taken at 1 h intervals (Figure 7a). Because each individual ping illuminates only a slice through the flare and not the entire volume (Figure 2b), these images contain the effects of spatial change in the volume imaged due to changes in the ship's heading (the blue line in Figure 7b) as well as temporal change in flare intensity. During the entire time period shown in Figure 7, the ship's position was stationary within a 50 m radius (Figure 1). During the first 6 h of observation, the

DOI:10.1190/INT-2021-0195.1

ship was intentionally allowed to rotate from 15° to 0° three times to sweep across the flare. The "bowtie" shown by dashed red lines on the backscatter slice at a depth of 1000 m in Figure 6 shows the approximate area ensonified by this rotation. During the last 2.5 h, a stationary heading was maintained, ensonifying a more limited sector of the flare (the solid red bowtie in Figure 6) but providing finer-scale temporal resolution. We also show the tide during this time period (the black line in Figure 7b) because others have noted an increase in flare intensity during a falling tide. At this site during this time period, which encompassed nearly one tidal cycle, flare intensity appeared minimum at 0630, approximately one-fourth cycle after high tide and then began to increase, although we note that the tidal height was smaller than the wave height during this time period and that our total observation period was much too short to resolve any potential tidal modulation overprinted by other effects.

To look more closely at the temporal variation during a 2.5 h period during which the vessel heading was nearly constant (Figure 7b), the data were processed in a manner analogous to that used to generate Figure 6 and supplemental animation S1. Instead of binning the data into bins in three spatial dimensions, however, the backscatter intensity values were binned into voxels with dimensions of horizontal and vertical distance within the swath of 15 m and a time period of 4 min to provide a high-resolution time series. The results are shown in Figure 8 as a series of vertical slices corresponding to supplemental animation S2. To illustrate the position of the MBES swath and the internal structure of each slice, horizontal slices at different depths are shown as a function of time and depth in Figure 9 with an X:Y scale ratio of 1:5. This time period provides an opportunity to look for events with short duration, although we must first evaluate whether changes represent true temporal changes or changes due to bubbles moving into or out of the plane of ensonification. It is likely that the abrupt appearance or disappearance of signals such as those marked by horizontal white arrows in Figure 8 represents secondary flares entering and exiting the swath of ensonification from the side.

We note a distinct pulse, labeled P1 in Figure 8, that can be tracked as it rises through the water column at a rate of 8–10 m/min (approximately 13–16 cm/s), which corresponds closely to the "dirty" (i.e., isolated from the ocean by a coasting of either hydrate or oil) bubble rise rate for bubbles of a size excited by the frequency of the EM122 (e.g., Leifer and Patro, 2002; Veloso et al., 2015; Biggs et al., 2019). We interpret the brightening and widening of the primary flare at 13:32 (supplemental animation S2) to represent a change in bubble flux. Figure 9 indicates that the MBES swath was stationary and sampling through the main part of the flare from 12:10 to 14:00 before drifting northeast between 14:00 and 14:30, supporting our interpretation of a change in flux, although we cannot rule out the possible contribution of plume drift relative to the MBES swath. The consistent appearance and indistinct upper and lower limits of the bright pulse outlined by the dotted line at 13:45 and 14:00 suggest upward translation of the pulse at a rate of 4–5 m/min, approximately half the rate of P1. These observations suggest that there are pulses of bubble release that last for tens of minutes as well as much shorter bursts.

Our results, as well as direct short-term visual observations of bubbles exiting the seafloor (e.g., Torres et al., 2002; Rehder et al., 2009; Fu et al., 2021), indicate that the approximately 1 h repeat time for previous acoustic surveys of temporal change in venting from deepwater (>500 m) methane vents in the Cascadia forearc (Kannberg et al., 2013; Philip et al., 2016; Römer et al., 2016) was not adequate to measure the rise rate of individual pulses. Our results also illustrate the complementary value of our two contrasting strategies for acoustic map-

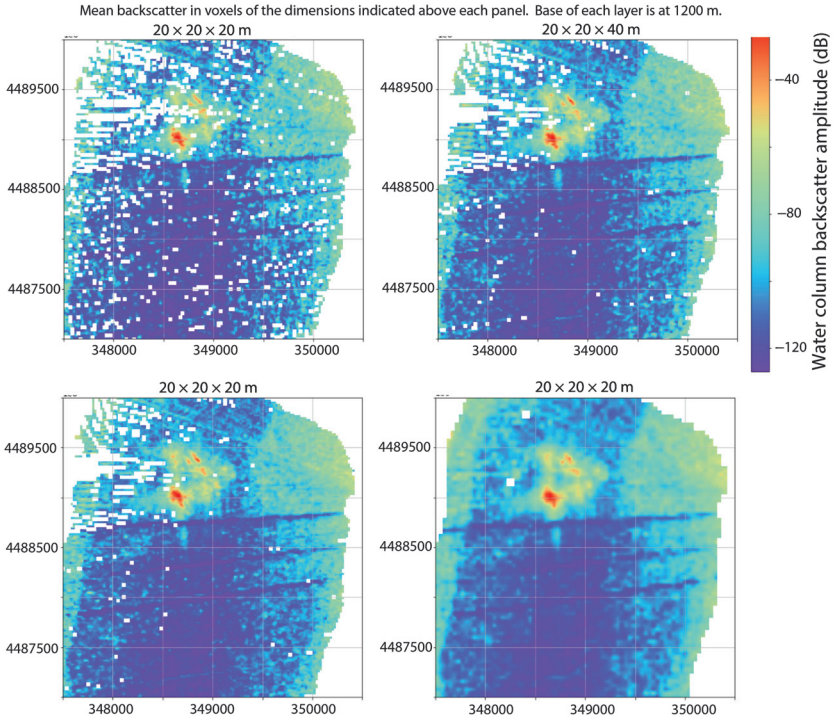

Figure 5. Example showing the empirical analysis used to determine the preferred voxel size for binning backscatter data acquired during transect 197. Backscatter data have been corrected for changes in the ship's heading, pitch, and roll. Binning in 20 × 20 × 20 m bins resulted in many holes in coverage. Increasing the vertical dimension of the bins to 40 m filled most of the holes, and increasing it further to 60 m did not significantly increase coverage compared to 40 m. Increasing the voxel size in the horizontal plane to 40 × 40 m resulted in some blurring of the images. Based on this analysis, we selected 20 × 20 × 40 m as the voxel size for Figure 6 and supplemental animation S1. The X and Y axes are in meters (UTM zone 10).

ping of flares using swath multibeam echosounder systems and the difficulty of capturing the large range of temporal variability of these dynamic systems.

ADCP and XBT observations

ADCP and XBT data acquired during the stationary observations and transect line 197 were examined to see if they could provide insights into flare behavior. At the beginning of the stationary observations, the current measured by the ADCP (Figure 10a) was to the west in the upper 50 m, to the south from 50 to 630 m, and to the east below 630 m. The current in the upper 280 m rotated to the southwest and the boundary between the current to the south and the underlying east-directed current shallowed from 630 to 400 m during the time period of our observations. This change in the current direction may be responsible for the apparent curvature of the secondary flares at approximately 600 m in Figure 8. Similar deflection of plumes by currents has been documented elsewhere (e.g., Philip et al., 2016).

The XBT data taken during acquisition of transect 197 (see Figure 1 for locations) are compared to more

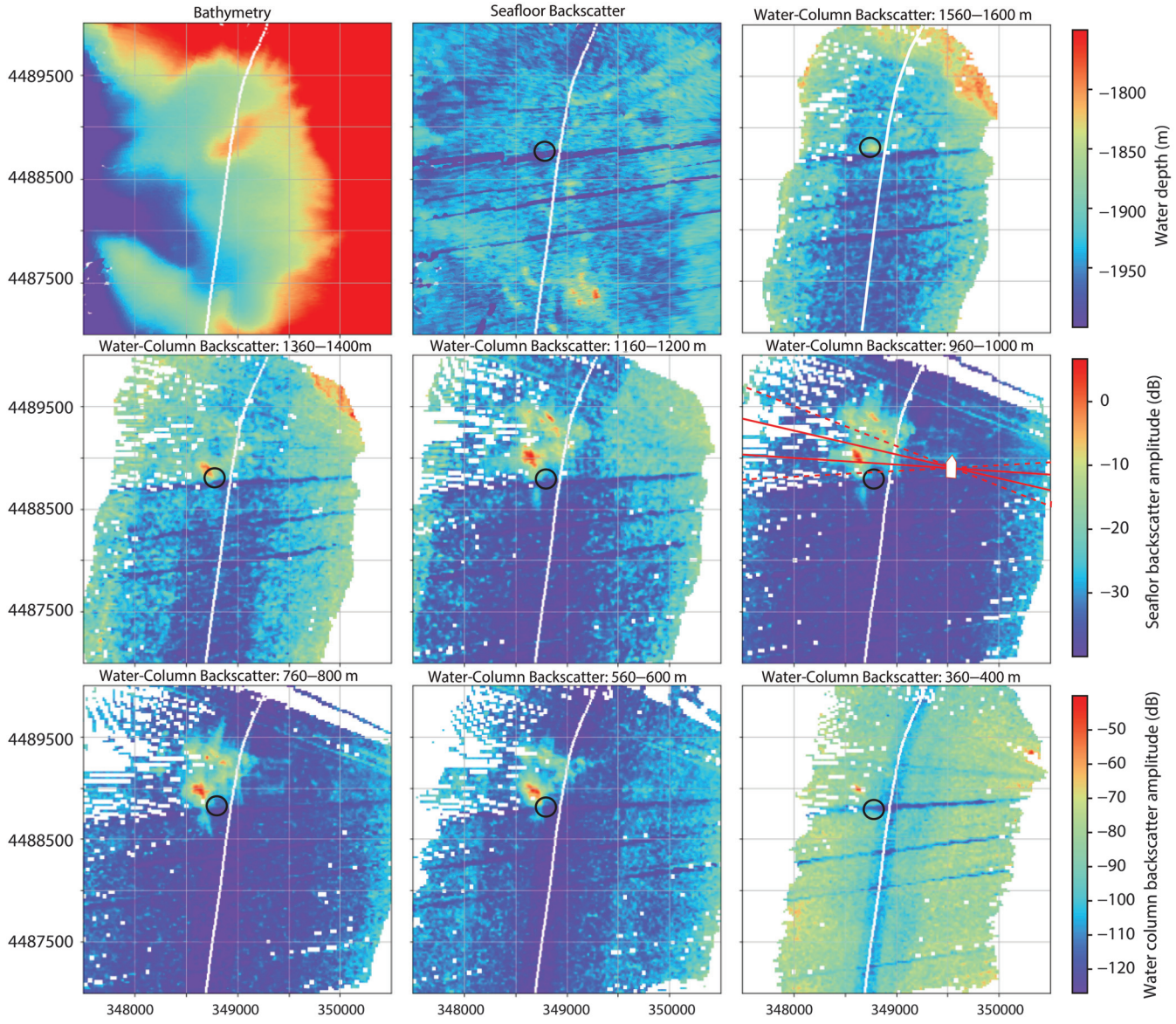

Figure 6. Maps of seafloor bathymetry, seafloor backscatter, and horizontal slices of acoustic backscatter summed more than 40 m thick layers as indicated in the title of each map for transect 197 (Figure 1) over the flare. The *X* and *Y* axes in meters (UTM zone 10). Voxel dimensions are 20 m in the *X* and *Y* directions and 40 m in depth. Color bars are amplitude scales for the bathymetry, seafloor reflectivity, and water column backscatter maps. All water column backscatter maps are shown with the same amplitude scale. Subhorizontal blue streaks on the backscatter maps are due to low-energy pings. The circle on each panel is the location of the flare at 1500–1600 m and is shown on each panel for reference. The solid white line indicates the vessel track. The red dashed lines on the 960–1000 m water-column backscatter map schematically show the sector that was imaged as the vessel (shown at approximately twice actual size) rotated while holding station during the time period shown in Figure 7. The solid red lines show the sector covered during the time period shown in Figure 8. See supplemental file S1 for an animation of this figure with 40 m intervals.

DOI:10.1190/INT-2021-0195.1

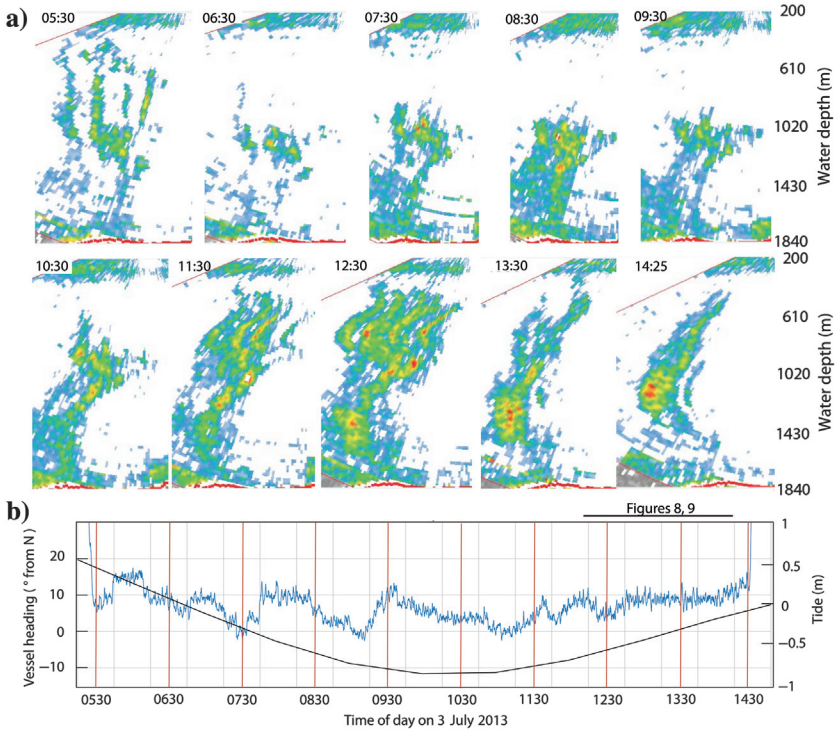

Figure 7. (a) Snapshots of the Eel Canyon flare at 1 h intervals when the ship was approximately stationary on 3 July 2013, displayed using QPS FMMidwater. The thick red line at the base of each snapshot is the seafloor return showing the position of the flare relative to the mound on the floor of the Eel Canyon slump. As for Figure 3, vertical and horizontal scales are similar, the red area indicates high intensity backscatter, and the white area represents an empirical threshold chosen to isolate the flare. Horizontal and amplitude scales are the same for each image. (b) Vessel heading and tidal height during this time period. Tidal height predicted by the model of Egbert and Erofeeva (2002). Horizontal bar above the graph shows the time period shown in Figures 8 and 9.

typical XBTs from the deepwater abyssal plain northwest of the Eel Canyon slump in Figure 10b and show an unusual profile of temperature as a function of depth beneath the sea surface in which the temperature decrease that defines the sound fixing and ranging (SOFAR) channel is muted and temperature shows relatively large oscillations with a wavelength of approximately 100 m. This may be due to turbulence generated by interaction of diurnal and semidiurnal tides with local seafloor topography in this region as observed and modeled by Musgrave et al. (2017), which may in turn contribute to the observed complex spatial and temporal variations in flare intensity.

Discussion

We introduce a new approach to processing MBES water column backscatter data in which the backscatter data are corrected for ship motion, including heading, pitch, and roll, and binned into voxels for interpretation as a 3D volume, analogous to a 3D seismic reflection or tomographic volume. Data are binned into voxels with three spatial dimensions when the ship is stationary. When the ship is transiting, one voxel dimension is time and the other two are

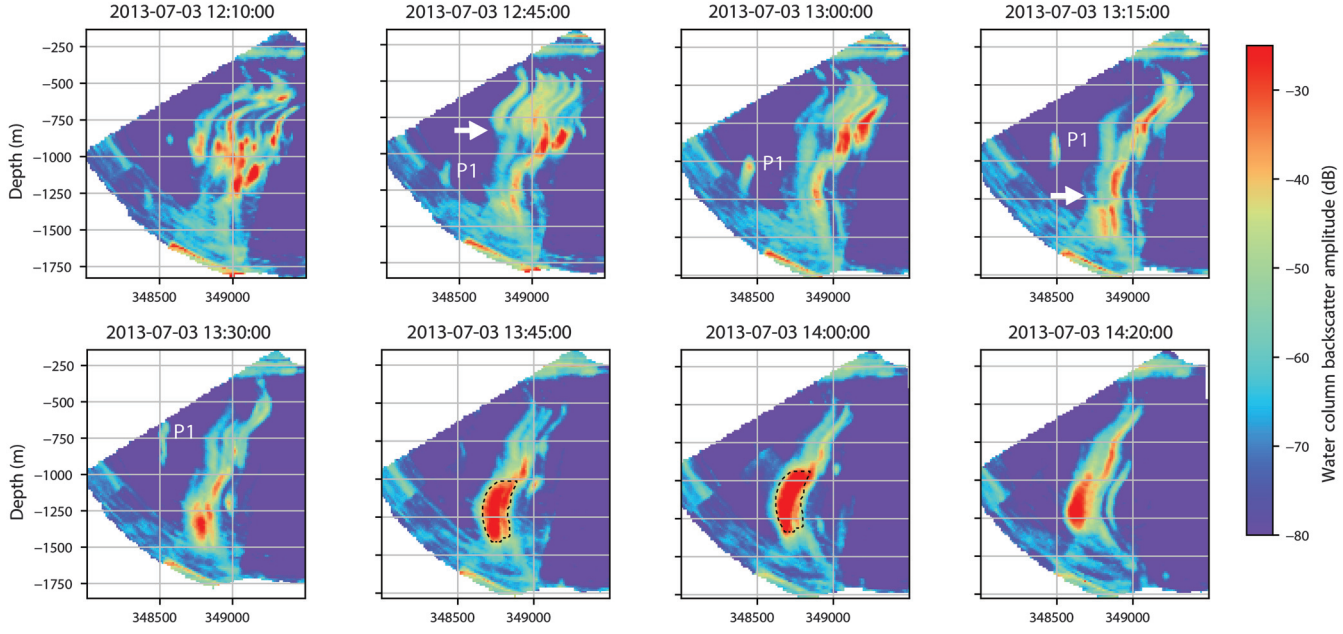

Figure 8. Vertical slices of backscatter binned into voxels with dimensions of 15 m in X and Z and 4 min in the direction perpendicular to the slice. Horizontal scale in meters (UTM zone 10). Slices are shown at approximately 15 min intervals from 1210 to 1420 on 3 July 2013. A backscatter "pulse" (labeled P1) can be traced from 12:45 to 13:30, when it rises out of the field of view. Horizontal white arrows show examples of abrupt vertical changes in backscatter intensity that likely result from bubble streams entering (at 12:10) or exiting (at 13:15) the ensonified swath. See A2 for an animation of this figure with one minute intervals from 12:00 to 14:10.

spatial. Horizontal backscatter slices (Figure 6 and supplemental animation S1) from a transect across the flare represent a static 3D view smoothed over the approximately 10 min it took to transit over the site. This view of the flare suggests the presence of a primary seafloor source with a diameter of approximately 40 m on the southwest edge of a circular region with a diameter of approximately 600 m from which several secondary flares emerge. Alternatively, secondary flares may develop from the primary flare in response to changing oceanographic conditions with decreasing depth. Although both processes may occur, and initial viewing of the data from the transect as a time series suggested the latter interpretation, the flare structure revealed through binning, averaging, and animation of the data from the transit across the flare leads us to prefer the explanation of a flare cluster with one primary and multiple secondary flares. The absence of a bright spot in the seafloor backscatter associated with this flare and the presence of bright spots elsewhere on the floor of the slump (Figure 6) support the inference from the high-resolution seafloor mapping of Gwiazda et al. (2016) that the locus of venting within the slump scar has changed on a millennial time scale.

The data show that the primary flare became wider and shifted in position as it rose from 1600 to 1200 m water depth. We speculate that this deflection is due to local turbulent flow induced by topography (Musgrave et al., 2017). Although we have no direct constraint on currents at that depth, anomalous XBT data taken at the same time as the MBES data show anomalous temperature structure inferred to result from topographically induced turbulence. Widening of the primary flare as it shallows may reflect an increased number of bubbles with decreasing depth in the size range that resonates when excited by acoustic energy at 12 kHz. Whether this increased number of bubbles is due to exsolution of gas from aqueous vent fluid entrained with the bubbles, expansion of bubbles due to decreasing pressure, or to a change in the flux of bub-

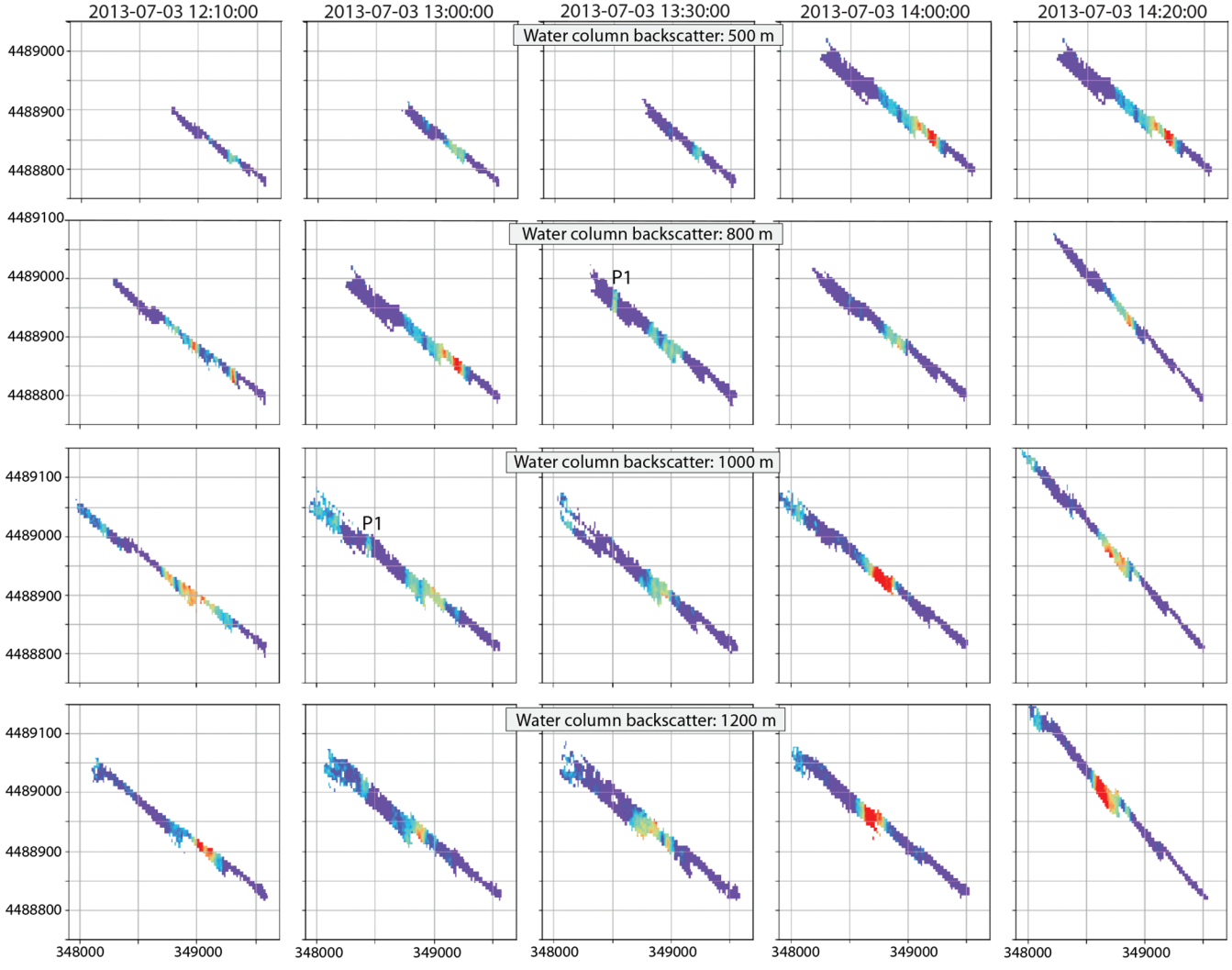

Figure 9. Horizontal slices at different depths corresponding to some of the times shown in Figure 8 to illustrate the width of the ensonified swath that was summed to generate the vertical slices shown in Figure 8 and supplemental animation S2. Data are binned into voxels with dimensions of 5 m in *X* and *Y* and 4 min in time. The *X* and *Y* axes in meters (UTM zone 10). Amplitude scale the same as in Figure 8. The swath is narrow compared to the dimensions of the flare.

DOI:10.1190/INT-2021-0195.1

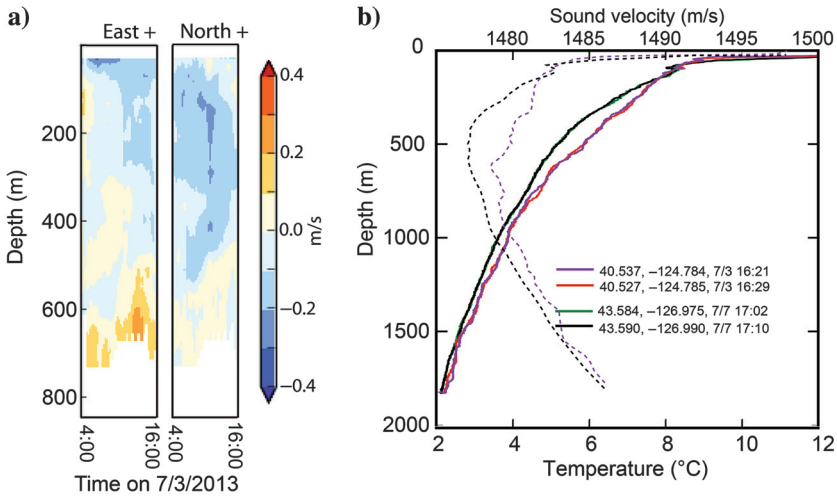

Figure 10. (a) ADCP data while the ship was acquiring data from a stationary position showing a change in current direction southwest greater than 300 m to east below 600–500 m. (b) Water temperature from XBT data acquired during AT2602. The profile shown by the purple line was acquired in the flare and the profile shown in red was acquired approximately 1 km to the south during transit 197 (locations shown by green stars in Figure 1). Also shown are data from the shelf northeast of the flare (green) and from the ocean basin northwest of the flare (two sites with nearly identical profiles shown in black). Dashed lines show the corresponding sound velocity profiles for the XBTs shown in purple and black, respectively, to illustrate the impact of the unusual temperature profile through the flare on the SOFAR channel.

bles exiting the seafloor cannot be resolved by a transit over the site and would require in situ time-series measurements at a range of frequencies. Secondary flares show deflection above 600–700 m consistent with the current direction measured by the ADCP.

Observations made while holding the ship stationary and offset from the flare complex reveal changes in the flare intensity over time scales of several minutes (Figure 8 and supplemental animation S2) within an approximately 50 m thick vertical slice through the flare. Although some of the changes we observe likely result from motion of the bubbles into and out of the slice, these can likely be identified by abrupt subhorizontal changes in intensity in the images. Some of the temporal variations appear to be due to pulses of bubbles that rise toward the surface. In particular, we can track a distinct high-amplitude backscatter pulse north of the primary flare that is observed from 12:26 to 13:20 with a rise rate of 8–10 m/min (13–16 cm/s). This rate is consistent with the rise rate of bubbles coated with a hydrate shell or oil film (Leifer and Patro, 2002; Veloso et al., 2015; Biggs et al., 2019). Because of changes in the size and shape of the pulse, we did not attempt to resolve a change in rise rate with depth and report only an approximate average rise rate. A larger pulse that appears in the primary flare near the seafloor at 13:32 seems to rise at a slower rate of 4–5 m/min.

Conclusions

Our results highlight the trade-off between temporal and spatial resolution when using shipboard multibeam soundings to image acoustic flares generated by methane bubbles. Imaging the entire affected volume containing bubbles with a narrow-band MBES requires transiting at a slow speed (<5 knots) for several kilometers over the flare (or acquiring a grid when mapping with a single beam). Each image of the flare therefore represents a "snapshot" of the flare averaged over tens of minutes, which can be repeated to produce a time series suitable for monitoring changes with a period of an hour or more. Short pulses of bubble release from the seafloor cannot be quantified with this approach. Imaging a flare from a stationary vantage point, on the other hand, can provide information on short-duration events (time scale of minutes), but provides only a narrow slice through a large, complex flare. Although it is difficult to distinguish changes in bubble flux from temporal changes due to motion of the flare relative to the slice, we argue that we were able to measure rise rates for at least one (and possibly two) distinct pulses from a stationary vantage point. A stationary vantage point thus complements a repeated transect strategy if the source of the flare has previously been identified.

Because a narrow-band MBES is sensitive to a limited range of bubble sizes and does not provide any ground-truth sampling of fluid composition, both data acquisition approaches provide a view of a bubble plume that is biased toward the bubble size that resonates at the system frequency, limiting the ability to resolve the flux of methane contained in bubbles that may have a range of sizes and whose size changes in response to decreasing pressure and loss of gas to diffusion as they rise through the water column. A comprehensive study of gas flux and the dynamics of seafloor gas venting requires a dedicated, multidisciplinary approach that includes acoustic, optical, and chemical observations that cover time scales of minutes to months or years with high spatial resolution within a volume large enough to encompass an entire vent system. Experiments of opportunity using MBES systems, however, can contribute new knowledge about seafloor gas vent dynamics and provide background information for planning more comprehensive efforts. Moreover, as more ships are equipped with sophisticated acoustic imaging systems, including those with multifrequency and 3D scanning (e.g., the Simrad StructureScan3D) capability, such opportunities should become more frequent.

Acknowledgments

We thank the captain and crew of the R/V Atlantis, who enabled acquisition of these data, and the many participants of AT26-02 who stood watch during the cruise. We thank reviewers D. Orange and two anonymous reviewers, and the associate editor, B. Phrampus, who provided very detailed and constructive reviews

that inspired us to modify our processing approach and interpretations. All acoustic multibeam and ADCP data used for this analysis have been archived at rvdata.org and are freely available. Multibeam data are also freely available from the Marine Geoscience Data System (www.marine-geo.org). Cruise AT26-02 was funded by the U.S. National Science Foundation as part of the Cascadia Initiative. This is PMEL contribution 5199. Tidal prediction from https://tpxows.azurewebsites.net.

Data and materials availability

Data associated with this research are available and can be accessed via the following URL: www.marine-geo.org.

References

Adam, J., D. Klaeschen, N. Kukowski, and E. Flueh, 2004, Upward delamination of Cascadia Basin sediment infill with landward frontal accretion thrusting caused by rapid glacial age material flux: Tectonics, **23**, TC3009, doi: 10.1029/2002TC001475.

AT26-02 Science Party, 2013, Cruise report Cascadia initiative: Year 3, Leg 3, 25 June 2013–9 July 2013, https://www.rvdata.us/search/cruise/AT26-02, accessed 19 December 2021.

Baumberger, T., R. W. Embley, S. G. Merle, M. D. Lilley, N. A. Raineault, and J. E. Lupton, 2018, Mantle-derived helium and multiple methane sources in gas bubbles of cold seeps along the Cascadia continental margin: Geochemistry, Geophysics, Geosystems, **19**, 4476–4486, doi: 10.1029/2018GC007859.

Berndt, C., T. Feseker, T. Treude, S. Krastel, V. Liebetrau, H. Niemann, V. J. Bertics, I. Dumke, K. Duennbier, B. Ferré, C. Graves, F. Gross, K. Hissmann, V. Huehnerbach, S. Krause, K. Lieser, J. Schauer, and L. Steinle, 2014, Temporal constraints on hydrate-controlled methane seepage off Svalbard: Science, **343**, 284–287, doi: 10.1126/science.1246298.

Biggs, B., J. J. Mountjoy, G. J. Crutchley, J. Townend, Y. Ladroit, J. Greinert, and C. McGovern, 2019, Seep-bubble characteristics and gas flow rates from a shallow-water, high-density seep field on the shelf-to-slope transition of the Hikurangi subduction margin: Marine Geology, **417**, 105985, doi: 10.1016/j.margeo.2019.105985.

Chadwick, W. W., S. G. Merle, N. J. Buck, J. W. Lavelle, J. A. Resing, and V. Ferrini, 2014, Imaging of CO_2 bubble plumes above an erupting submarine volcano, NW Rota-1, Mariana Arc: Geochemistry, Geophysics, Geosystems, **15**, 4325–4342, doi: 10.1002/2014GC005543.

Clay, C. S., and H. Medwin, 1977, Acoustical oceanography: Principles and applications: John Wiley and Sons.

Dickens, G. R., 2011, Down the rabbit hole: Toward appropriate discussion of methane release from gas hydrate systems during the Paleocene-Eocene thermal maximum and other past hyperthermal events: Climate of the Past Discussions, **7**, 831–846, doi: 10.5194/cp-7-831-2011.

Egbert, G. D., and S. Y. Erofeeva, 2002, Efficient inverse modeling of barotropic ocean tides: Journal of Atmospheric and Oceanic Technology, **19**, 183–204, doi: 10.1175/1520-0426(2002)019<0183:EIMOBO>2.0.CO;2.

Fisher, M. A., R. D. Hyndman, S. Y. Johnson, T. M. Brocher, R. S. Crosson, R. E. Wells, A. J. Calvert, and U. S. ten Brink, 2005, Crustal structure and earthquake hazards of the subduction zone in southwestern British Columbia and western Washington: U. S. Geological Survey Professional Paper 1661-C, 28 pages and 3 plates, http://pubs.usgs.gov/pp/pp1661-C, accessed 19 December 2021.

Fu, X., W. F. Waite, and C. D. Ruppel, 2021, Hydrate formation on marine seep bubbles and the implications for water column methane dissolution: Journal of Geophysical Research Oceans, **126**, e2021JC017363, doi: 10.1029/2021JC017363.

Gardner, J. V., M. Malik, and S. Walker, 2009, Plume 1400 meters high discovered at the seafloor off the northern California margin: Eos, Transactions American Geophysical Union, **90**, 275–275, doi: 10.1029/2009EO320003.

Godfrey, N. J., A. S. Meltzer, S. L. Klemperer, A. M. Tréhu, B. Leitner, S. H. Clarke, Jr., and A. Ondrus, 1998, Evolution of the Gorda Escarpment, San Andreas fault and Mendocino triple junction from multichannel seismic data collected across the northern Vizcaino block, offshore northern California: Journal of Geophysical Research, Solid Earth, **103**, 23813–23825, doi: 10.1029/98JB02138.

Gulick, S. P., A. M. Meltzer, and S. H. Clarke Jr., 1998, Seismic structure of the southern Cascadia subduction zone and accretionary prism north of the Mendocino triple junction: Journal of Geophysical Research, Solid Earth, **103**, 27207–27222, doi: 10.1029/98JB02526.

Gwiazda, R., C. K. Paull, D. W. Caress, T. Lorenson, P. G. Brewer, E. T. Peltzer, P. M. Walz, K. Anderson, and E. Lundsten, 2016, Eel canyon slump scar and associated fluid venting, *in* G. Lamarche, J. Mountjoy, S. Bull, T. Hubble, S. Krastel, E. Lane, A. Micallef, L. Moscardelli, C. Mueller, I. Pecher, and S. Woelz, eds., Submarine mass movements and their consequences: Advances in natural and technological hazards research: Springer, **41**, 411–418.

Heeschen, K. U., R. W. Collier, M. A. de Angelis, E. Suess, G. Rehder, P. Linke, and G. P. Klinkhammer, 2005, Methane sources, distributions, and fluxes from cold vent sites at Hydrate Ridge, Cascadia Margin: Global Biogeochemical Cycles, **19**, GB2016, doi: 10.1029/2004GB002266.

Heeschen, K. U., A. M. Tréhu, R. W. Collier, E. Suess, and G. Rehder, 2003, Distribution and height of methane bubble plumes on the Cascadia Margin characterized by acoustic imaging: Geophysical Research Letters, **30**, 1643, doi: 10.1029/2003GL016974.

Henstock, T. J., and A. Levander, 2003, Structure and seismotectonics of the Mendocino Triple Junction,

California: Journal of Geophysical Research, Solid Earth, **108**, 2060, doi: 10.1029/2001JB000902.

Hill, J. C., J. T. Watt, D. S. Brothers, and J. W. Kluesner, 2020, Submarine canyons, slope failures and mass transport processes in southern Cascadia: Geological Society, London, Special Publications, **500**, 453–475, doi: 10.1144/SP500-2019-169.

Hornafius, J. S., D. Quigley, and B. P. Luyendyk, 1999, The world's most spectacular marine hydrocarbon seeps (Coal Oil Point, Santa Barbara Channel, California): Quantification of emissions: Journal of Geophysical Research, Oceans, **104**, 20703–20711, doi: 10.1029/1999JC900148.

Hovland, M., D. Lysne, and M. Whiticar, 1995, Gas hydrate and sediment gas composition, Hole 892A, *in* B. Carson, G. K. Westbrook, R. J. Musgrave, and E. Suess, eds., Proceedings of the Ocean Drilling Program, Scientific Results, **146**, 151–162.

Hyndman, R. D., K. Wang, T. Yuan, and G. D. Spence, 1993, Tectonic sediment thickening, fluid expulsion, and the thermal regime of subduction zone accretionary prisms: The Cascadia margin off Vancouver Island: Journal of Geophysical Research, Solid Earth, **98**, 21865–21876, doi: 10.1029/93JB02391.

Kannberg, P. K., A. M. Tréhu, S. D. Pierce, C. K. Paull, and D. W. Caress, 2013, Temporal variation of methane flares in the ocean above Hydrate Ridge, Oregon: Earth and Planetary Science Letters, **368**, 33–42, doi: 10.1016/j.epsl.2013.02.030.

Leifer, I., and R. K. Patro, 2002, The bubble mechanism for methane transport from the shallow sea bed to the surface: A review and sensitivity study: Continental Shelf Research, **22**, 2409–2428, doi: 10.1016/S0278-4343(02)00065-1.

MacDonald, I. R., O. Garcia-Pineda, A. Beet, S. Daneshgar Asl, L. Feng, G. Graettinger, D. French-McCay, J. Holmes, C. Hu, F. Huffer, I. Leifer, F. Muller-Karger, A. Solow, M. Silva, and G. Swayze, 2015, Natural and unnatural oil slicks in the Gulf of Mexico: Journal of Geophysical Research, Oceans, **120**, 8364–8380, doi: 10.1002/2015JC011062.

MacDonald, I. R., I. Leifer, R. Sassen, P. Stine, R. Mitchell, and N. Guinasso Jr., 2002, Transfer of hydrocarbons from natural seeps to the water column and atmosphere: Geofluids, **2**, 95–107, doi: 10.1046/j.1468-8123.2002.00023.x.

Merewether, R., M. S. Olsson, and P. Lonsdale, 1985, Acoustically detected hydrocarbon plumes rising from 2-km depths in Guaymas Basin, Gulf of California: Journal of Geophysical Research, Solid Earth, **90**, 3075–3085, doi: 10.1029/JB090iB04p03075.

Merle, S. G., R. W. Embley, H. P. Johnson, T. K. Lau, B. Phrampus, N. Raineault, and L. Gee, 2021, Distribution of methane plumes on Cascadia Margin and implications for the landward limit of methane hydrate stability: Frontiers in Earth Science, **9**, 531714, doi: 10.3389/feart.2021.531714.

Musgrave, R. C., J. A. MacKinnon, R. Pinkel, A. F. Waterhouse, J. Nash, and S. M. Kelly, 2017, The influence of subinertial internal tides on near-topographic turbulence at the Mendocino Ridge: Observations and modeling: Journal of Physical Oceanography, **47**, 2139–2154, doi: 10.1175/JPO-D-16-0278.1.

NA095 cruise report, 2018, Cascadia Margin, cruise report, https://www.pmel.noaa.gov/eoi/Cascadia/Cascadia-Margin-Cruise-Report-2018.pdf.

Paull, C. K., D. W. Caress, H. Thomas, E. Lundsten, K. Anderson, R. Gwiazda, M. Riedel, M. McGann, and J. C. Herguera, 2015, Seafloor geomorphic manifestations of gas venting and shallow subbottom gas hydrate occurrences: Geosphere, **11**, 491–513, doi: 10.1130/GES01012.1.

Philip, B. T., A. R. Denny, E. A. Solomon, and D. S. Kelley, 2016, Time-series measurements of bubble plume variability and water column methane distribution above Southern Hydrate Ridge, Oregon: Geochemistry, Geophysics, Geosystems, **17**, 1182–1196, doi: 10.1002/2016GC006250.

Phrampus, B. J., R. N. Harris, and A. M. Tréhu, 2017, Heat flow bounds over the Cascadia margin derived from bottom simulating reflectors and implications for thermal models of subduction: Geochemistry, Geophysics, Geosystems, **18**, 3309–3326, doi: 10.1002/2017GC007077.

Prouty, N. G., D. Sahy, C. D. Ruppel, E. B. Roark, D. Condon, S. Brooke, S. W. Ross, and A. W. J. Demopoulos, 2016, Insights into methane dynamics from analysis of authigenic carbonates and chemosynthetic mussels at newly-discovered Atlantic Margin seeps: Earth and Planetary Science Letters, **449**, 332–344, doi: 10.1016/j.epsl.2016.05.023.

Razaz, M., D. Di Iorio, B. Wang, S. D. Asl, and A. M. Thurnherr, 2020, Variability of a natural hydrocarbon seep and its connection to the ocean surface: Scientific Reports, **10**, 1–13, doi: 10.1038/s41598-020-68807-4.

Rehder, G., I. Liefer, P. G. Brewer, G. Friedrich, and E. T. Peltzer, 2009, Controls on methane bubble dissolution inside and outside the hydrate stability field from open ocean field experiments and numerical modeling: Marine Chemistry, **114**, 19–30, doi: 10.1016/j.marchem.2009.03.004.

Riedel, M., M. Scherwath, M. Römer, M. Veloso, M. Heesemann, and G. D. Spence, 2018, Distributed natural gas venting offshore along the Cascadia margin: Nature Communications, **9**, 1–14, doi: 10.1038/s41467-018-05736-x.

Römer, M., M. Riedel, M. Scherwath, M. Heesemann, and G. D. Spence, 2016, Tidally controlled gas bubble emissions: A comprehensive study using long-term monitoring data from the NEPTUNE cabled observatory offshore Vancouver Island: Geochemistry, Geophysics, Geosystems, **17**, 3797–3814, doi: 10.1002/2016GC006528.

Ruppel, C. D., and J. D. Kessler, 2017, The interaction of climate change and methane hydrates: Reviews of Geophysics, **55**, 126–168, doi: 10.1002/2016RG000534.

Salmi, M. S., H. P. Johnson, I. Leifer, and J. E. Keister, 2011, Behavior of methane seep bubbles over a pockmark on

the Cascadia continental margin: Geosphere, **7**, 1273–1283, doi: 10.1130/GES00648.1.

Suess, E., M. E. Torres, G. Bohrmann, R. W. Collier, D. Rickert, C. Goldfinger, P. Linke, A. Heuser, H. Sahling, K. Heeschen, C. Jung, K. Nakamura, J. Greinert, O. Pfannkuche, A. Trehu, G. Klinkhammer, M. J. Whiticar, A. Eisenhauer, B. Teichert, and M. Elvert, 2001, Sea floor methane hydrates at Hydrate Ridge, Cascadia margin: American Geophysical Union, Geophysical Monograph, **124**, 87–98.

Teichert, B. M., A. Eisenhauer, G. Bohrmann, A. Haase-Schramm, B. Bock, and P. Linke, 2003, U/Th systematics and ages of authigenic carbonates from Hydrate Ridge, Cascadia Margin: Recorders of fluid flow variations: Geochimica et Cosmochimica Acta, **67**, 3845–3857, doi: 10.1016/S0016-7037(03)00128-5.

Toomey, D. R., R. M. Allen, A. H. Barclay, S. W. Bell, P. D. Bromirski, R. L. Carlson, X. Chen, J. A. Collins, R. P. Dziak, B. Evers, D. W. Forsyth, P. Gerstoft, E. E. E. Hooft, D. Livelybrooks, J. A. Lodewyk, D. S. Luther, J. J. McGuire, S. Y. Schwartz, M. Tolstoy, A. M. Tréhu, M. Weirathmueller, and W. S. D. Wilcock, 2014, The Cascadia Initiative: A sea change in seismological studies of subduction zones: Oceanography, **27**, 138–150, doi: 10.5670/oceanog.2014.49.

Torres, M. E., R. W. Embley, S. G. Merle, A. M. Tréhu, R. W. Collier, E. Suess, and K. U. Heeschen, 2009, Methane sources feeding cold seeps on the shelf and upper continental slope off central Oregon, USA: Geochemistry, Geophysics, Geosystems, **10**, Q11003, doi: 10.1029/2009GC002518.

Torres, M. E., J. McManus, D. Hammond, M. A. de Angelis, K. Heeschen, S. Colbert, M. D. Tryon, K. M. Brown, and E. Suess, 2002, Fluid and chemical fluxes in and out of sediments hosting methane hydrate deposits on Hydrate Ridge, OR — I: Hydrological provinces: Earth and Planetary Science Letters, **201**, 525–540, doi: 10.1016/S0012-821X(02)00733-1.

Torres, M. E., K. Wallmann, A. M. Tréhu, G. Bohrmann, W. S. Borowski, and H. Tomaru, 2004, Gas hydrate growth, methane transport, and chloride enrichment at the southern summit of Hydrate Ridge, Cascadia margin off Oregon: Earth and Planetary Science Letters, **226**, 225–241, doi: 10.1016/j.epsl.2004.07.029.

Tréhu, A. M., P. B. Flemings, N. L. Bangs, J. Chevallier, E. Gràcia, J. E. Johnson, C. S. Liu, X. Liu, M. Riedel, and M. E. Torres, 2004, Feeding methane vents and gas hydrate deposits at south Hydrate Ridge: Geophysical Research Letters, **31**, L23310, doi: 10.1029/2004GL021286.

Tréhu, A. M., G. Lin, E. Maxwell, and C. Goldfinger, 1995, A seismic reflection profile across the Cascadia subduction zone offshore central Oregon: New constraints on methane distribution and crustal structure: Journal of Geophysical Research, Solid Earth, **100**, 15101–15116, doi: 10.1029/95JB00240.

Tréhu, A. M., C. Ruppel, G. R. Dickens, M. Holland, M. E. Torres, T. S. Collett, D. Goldberg, M. Riedel, and P. Schultheiss, 2006, Gas hydrates in marine sediments: Lessons from scientific drilling: Oceanography, **19**, 124–142, doi: 10.5670/oceanog.2006.11.

Tréhu, A. M., M. E. Torres, G. F. Moore, E. Suess, and G. Bohrmann, 1999, Temporal and spatial evolution of a gas hydrate-bearing accretionary ridge on the Oregon continental margin: Geology, **27**, 939–942, doi: 10.1130/0091-7613(1999)027<0939:TASEOA>2.3.CO;2.

Tryon, M. D., K. M. Brown, M. E. Torres, A. M. Tréhu, J. McManus, and R. W. Collier, 1999, Measurements of transience and downward flow near episodic methane gas vents, Hydrate Ridge, Cascadia: Geology, **27**, 1075–1078, doi: 10.1130/0091-7613(1999)027<1075:MOTADF>2.3.CO;2.

Veloso, M., J. Greinert, J. Mienert, and M. De Batist, 2015, A new methodology for quantifying bubble flow rates in deep water using splitbeam echosounders: Examples from the Arctic offshore NW-S valbard: Limnology and Oceanography: Methods, **13**, 267–287, doi: 10.1002/lom3.10024.

Wang, K., and A. M. Tréhu, 2016, Invited review paper: Some outstanding issues in the study of great megathrust earthquakes — The Cascadia example: Journal of Geodynamics, **98**, 1–18, doi: 10.1016/j.jog.2016.03.010.

Westbrook, G. K., K. E. Thatcher, E. J. Rohling, A. M. Piotrowski, H. Pälike, A. H. Osborne, E. G. Nisbet, T. A. Minshull, M. Lanoiselle, R. H. James, V. Hühnerbach, D. Green, R. E. Fisher, A. J. Crocker, A. Chabert, C. Bolton, A. Beszcyzynaska-Moller, and A. Aquilla, 2009, Escape of methane gas from the seabed along the West Spitsbergen continental margin: Geophysical Research Letters, **36**, L15608, doi: 10.1029/2009GL039191.

Biographies and photographs of the authors are not available.